DTU Library

Crystallization and OFET Performance of a Hydrogen-Bonded Quaterthiophene

Gebers, Jan; Özen, Bilal; Hartmann, Lucia; Schaer, Michel; Suarez, Stéphane; Bugnon, Philippe; Scopelliti, Rosario; Steinrück, Hans-Georg; Konovalov, Oleg; Magerl, Andreas

Total number of authors:
15

[Link back to DTU Orbit](https://orbit.dtu.dk)

Accepted Article

Title: Crystallization and OFET Performance of a Hydrogen-Bonded Quaterthiophene

Authors: Jan Gebers, Bilal Özen, Lucia Hartmann, Michel Schaer, Stéphane Suarez, Philippe Bugnon, Rosario Scopelliti, Hans-Georg Steinrück, Oleg Konovalov, Andreas Magerl, Martin Brinkmann, Riccardo Petraglia, Piotr de Silva, Clémence Corminboeuf, and Holger Frauenrath

WILEY-VCH

FULL PAPER

Crystallization and OFET Performance of a Hydrogen-Bonded Quaterthiophene

Jan Gebers,[a]‡ Bilal Özen,[a]‡ Lucia Hartmann,[a] Michel Schaer,[a] Stéphane Suàrez,[a] Philippe Bugnon,[b] Rosario Scopelliti,[c] Hans-Georg Steinrück, [d,e] Oleg Konovalov,[f] Andreas Magerl,[d] Martin Brinkmann,[g] Riccardo Petraglia,[h] Piotr de Silva,[h,i] Clémence Corminboeuf,[h] and Holger Frauenrath,*[a]

Abstract: Crystalline thin films of π-conjugated molecules are relevant as the active layers in organic electronic devices. Therefore, materials with enhanced control over the supramolecular arrangement, crystallinity, and thin film morphology are desirable. Here, we report that hydrogen-bonded substituents serve as additional structure-directing elements that positively affect crystallization, thin film morphology, and device performance of p-type organic semiconductors. We observed that a quaterthiophene diacetamide exhibited a denser packing than other quaterthiophenes in the single-crystal structure and, as a result, displayed enhanced intermolecular electronic interactions. This feature was preserved in crystalline thin films that exhibited a layer-by-layer morphology with large domain sizes and high internal order. As a result, organic field-effect transistors of these polycrystalline thin films showed mobilities

in the range of the best mobilities values reported for single-crystalline quaterthiophenes. The use of hydrogen-bonded groups may, thus, provide an avenue for organic semiconducting materials with improved morphology and performance.

Introduction

Crystalline thin films of π-conjugated molecules have emerged as efficient semiconductors in electronic devices such as organic field-effect transistors (OFETs),[1–4] photovoltaics,[5] light-emitting diodes,[6] chemical sensors,[7] and other electronic devices.[8,9] Both a large intermolecular π-overlap and macroscopically continuous charge percolation paths are required for good semiconducting properties. Therefore, materials with an enhanced control over the supramolecular arrangement of the π-conjugated segments within the crystal structure, the size of the crystalline domains, and the thin film morphology are desirable. To this end, the modification of the π-conjugated cores themselves, variation of molecular architectures (for instance, linear, cyclic, or branched cores), decoration with non-functional solubilizing groups (mostly linear or branched alkyl substituents), or the application of different processing techniques (such as sublimation, spin- or dip-coating, or guided crystallization) have been explored.[2,3,10,11] It has recently been demonstrated that a high degree of short-range intermolecular order is an important performance parameter in the case of polymer semiconductors.[12] Hydrogen-bonded templates and substituents have proven to be useful structure-directing groups to establish strong and specific intermolecular interactions that guide crystallization or supramolecular self-organization.[13–19] Nevertheless, the effect of hydrogen-bonded functional groups on the structure and properties of organic semiconductors in the solid-state has not been extensively investigated until recently, supposedly because they were suspected to serve as trap states.[20] The effect of hydrogen-bonded groups on the charge-carrier mobility of certain sexithiophenes [21] and naphthalene diimides [22] in OFETs was investigated but no improvement in device performance was observed. An α,ω-hydroxypropyl-substituted sexithiophene was found to exhibit enhanced layer-by-layer thin film growth and was successfully used in thin film devices.[23] Hydrogen bonding has been applied in the solution-phase self-assembly of oligothiophene derivatives into one-dimensional aggregates;[24–31] but while field-effect devices have been used in some cases to determine the properties of the resulting aggregates, the specific role of hydrogen bonding for macroscopic device performance was not systematically investigated in these studies.

Only recently, it was shown that hydrogen bonding positively affected the thin film packing of naphthalene diimide and diketopyrrolopyrrole (DPP) derivatives.[32,33] According to computations on perylene bisimides, hydrogen bonding

[a]   Dr. J. Gebers, B. Özen, Dr. L. Hartmann, M. Schaer, Dr. S. Suàrez,
        Prof. H. Frauenrath
        Institute of Materials
        École Polytechnique Fédérale de Lausanne (EPFL)
        EPFL–STI–IMX–LMOM, MXG 135, Station 12, 1015 Lausanne,
        Switzerland
        E-mail: holger.frauenrath@epfl.ch
[b]   P. Bugnon
        Institute of Condensed Matter Physics
        École Polytechnique Fédérale de Lausanne (EPFL)
        EPFL–PH J0 491, Station 3, 1015 Lausanne, Switzerland
[c]   Dr. R. Scopelliti
        Institute of Chemical Sciences and Engineering
        École Polytechnique Fédérale de Lausanne (EPFL)
        EPFL–BCH 2111, Batochime UNIL, Avenue Forel 2, 1015
        Lausanne, Switzerland
[d]   Dr. H.-G. Steinrück, Prof. A. Magerl
        University of Erlangen-Nürnberg
        Crystallography and Structural Physics,
        Staudtstr. 3, 91058 Erlangen, Germany
[e]   present address:
        Technische und Makromolekulare Chemie,
        Universität Paderborn
        Warburger Str. 100,33098 Paderborn, Germany
[f]   Dr. O. Konovalov
        European Synchrotron Radiation Facility (ESRF)
        6 rue Jules Horowitz, BP220, 38043 Grenoble Cedex, France
[g]   Dr. M. Brinkmann
        Université de Strasbourg
        Institut Charles Sadron CNRS
        Rue du Loess 23, 67034 Strasbourg, France
[h]   Dr. R. Petraglia, Dr. P. de Silva, Prof. C. Corminboeuf
        Institute of Chemical Sciences and Engineering
        École Polytechnique Fédérale de Lausanne (EPFL)
        EPFL–BCH 5312, Batochime UNIL, Avenue Forel 2, 1015 Lausanne
        Switzerland
[i]   present address:
        Department of Energy Conversion and Storage,
        Technical University of Denmark
        Anker Engelunds Vej 301, 2800 Kongens Lyngby, Denmark

        ‡ Both authors contributed equally to this publication.

        Supporting information for this article is given via a link at the end of
        the document.

interactions should have a beneficial effect on device performance.[34] Consistent with these reports, experimental results for n-type semiconductors have indicated no adverse effect of hydrogen bonding on transport properties.[35] Würthner and coworkers even found that the *N*-unsubstituted octachloroperylene bisimide was an efficient n-type organic semiconductor, as a consequence of the dense "brickwork" crystal structure induced by the hydrogen-bonded imides.[36] A similar beneficial effect of hydrogen bonding has also been observed for low band gap polymers with hydrogen-bonded side chains.[37] Notably, Głowacki et al. systematically studied hydrogen-bonded π-conjugated compounds has charge-transport materials in organic field-effect transistors.[38,39] For example, that OFETs printed from intermolecularly N-H ⋯ O=C hydrogen-bonded heteroacene pigments showed field-effect mobilities as high as 1.5 cm^2 V^{-1} s^{-1} and good device life times even under ambient conditions.[40,41] In all of these experimental examples, the hydrogen bonding sites were part of and in plane with the respective π-conjugated systems.

Here, we demonstrate that terminal hydrogen-bonded substituents may be used to guide and improve crystallization of calamitic π-conjugated molecules, tailor their thin film morphology and improve the device performance of the resulting p-type organic semiconductors. We observed that the crystalline quaterthiophene diacetamide **1** (Figure 1*a*) exhibited a noticeably denser packing of the molecules in the unit cell and improved π-interactions as compared with other quaterthiophenes,[42–44] including the closely related quaterthiophene diacetate **2**. We found this feature to be preserved in the structure of crystalline thin films, whose morphology and domain sizes may be tuned depending on the deposition conditions and dielectric surface pre-treatment. As a result, field-effect transistors fabricated from these polycrystalline thin films revealed average mobilities of up to 0.18 cm^2 V^{-1} s^{-1}, which is almost two orders of magnitude higher than those of than the reference compound **2** and, notably, in the same range as the best mobilities reported for a single-crystalline quaterthiophene specimens to date.[45–47] The use of hydrogen-bonded side groups as an additional structure-directing element may, thus, provide a general pathway towards novel organic and polymer semiconducting materials with improved morphology and performance.

Results and Discussion

Single-Crystal X-Ray Structure

In the quaterthiophene diacetamide **1**,[48] the terminal acetamide functions offer the possibility of intermolecular N–H⋯O=C hydrogen bonding. Solid-state infrared (IR) spectroscopy of **1** revealed strongly, resonance-enhanced amide hydrogen bonding at room temperature with characteristic amide A, I, and II absorption bands at 3280, 1636, and 1550 cm^{-1}, respectively, similar to the those observed in crystalline domains of polyamides (Supplementary Figure S1).[49] The amide groups are linked to the π-conjugated core via a short flexible spacer to decouple the respective packing requirements. Hydrogen bonding is indeed observed in the single-crystal structure of **1** and appears to induce an overall tighter packing of the quaterthiophene cores. This results in a noticeably smaller unit cell and increased π-interactions of neighboring molecules, as compared with the non-hydrogen-bonded quaterthiophene

diacetate **2** and other quaterthiophene derivatives without hydrogen-bonded lateral substituents. **1** crystallized as flat needles or elongated platelets (Figure 1b) in the triclinic $P\bar{1}$ space group (a = 5.89 Å, b = 7.65 Å, c = 25.78 Å, α = 97.4°, β = 93.8°, and γ = 91.1°), while monoclinic or orthorhombic unit cells were typically observed for other representative examples of quaterthiophenes such as the quaterthiophene diacetate **2**, the low-temperature polymorph of α-quaterthiophene (α-4T),[42] α,ω-dimethylquaterthiophene (DM4T),[43] or α,ω-dihexylquaterthiophene (DH4T).[44]
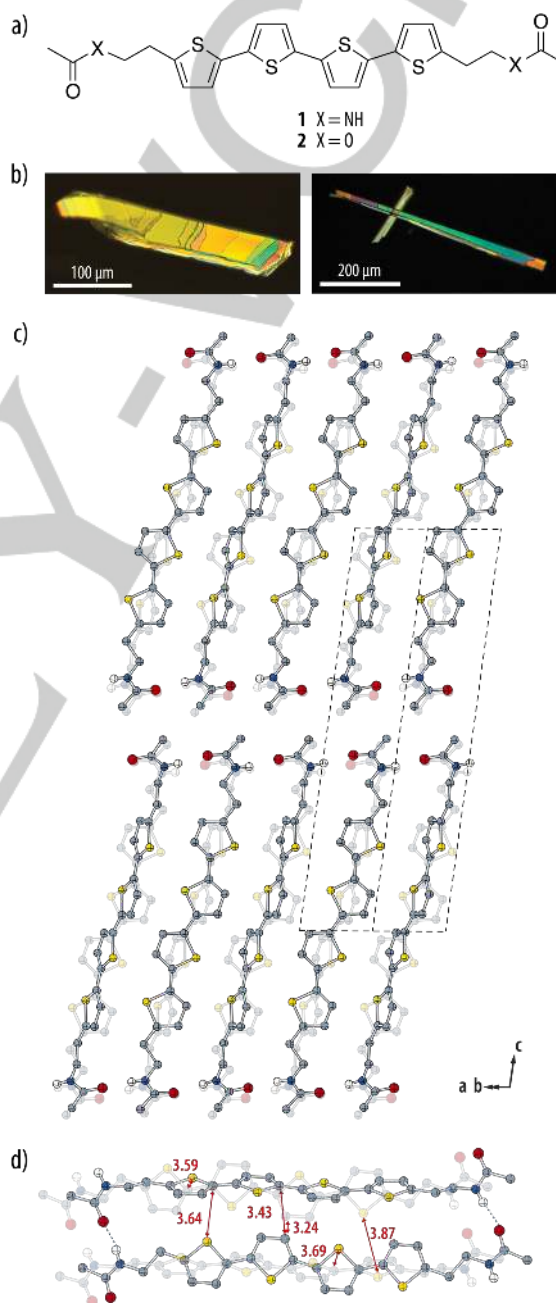
Figure 1. *a*) Molecular structures of the quaterthiophene bisacetamide **1** and the corresponding diacetate **2**. *b*) Polarized optical micrographs (under crossed polarizers) of single crystals of **1** *c,d*) ball-and-stick representations of the single-crystal X-ray structure of quaterthiophene diacetamide **1** (CCDC 976399) with a view along the crystallographic [110] axis, and an illustration of the C⋯C, C⋯S, and S⋯S short contacts (in Ångstroms) between edge-to-face and parallel-displaced neighboring pairs of molecules (all hydrogen atoms except the amide hydrogens omitted for clarity).

Table 1. Comparison of the crystal structure of **1** (CCDC 976399) with the structures of the quaterthiophene diacetate **2** (CCDC 1043812), the low temperature polymorph of α-4T,[42] α,ω-dimethylquaterthiophene (DM4T),[43] and α,ω-dihexylquaterthiophene (DH4T).[44]

property	1	2	α-4T	DM4T	DH4T
space group	$P\bar{1}$	$P\,2_1/c$	$P\,2_1/c$	$P\,bca$	$P\,2_1/a$
crystal system	triclinic	monoclinic	monoclinic	orthorhombic	monoclinic
a (Å)	5.89	5.88	6.09	7.71	6.05
b (Å)	7.65	9.01	7.86	5.94	7.81
c (Å)	25.8	22.09	30.5	36.0	28.53
α (°)	97.4	90	90	90	90
β (°)	93.8	91.8	91.8	90	92.4
γ (°)	91.1	90	90	90	90
herringbone angle[a]	60.0°	60.8°	63.1°	62.1°	62.8°
tilt angle[b]	23.9 / 24.2°	35.0°	24.8°	23.3°	23.9°
ab area/4T[c] (Å²)	22.5	26.5	23.9	22.9	23.6
volume/4T[d] (Å³)	291	308	307	297	306

[a] Angle between the mean planes of two edge-to-face interacting quaterthiophene cores; [b] angle of the quaterthiophene's long axis with respect to the layer normal; [c] area span between the a and b vectors of the unit cell divided by the number of quaterthiophenes in this plane; [d] volume per quaterthiophene core calculated using the ab-area, tilt angle and distance between the α- and ω-carbons of the quaterthiophene.

The packing of **1** (Figure 1*c*), **2** (Supplementary Figure S2), and the other quaterthiophenes shared several common features (Table 1). In all cases, the quaterthiophene cores were arranged into layers along the *ab* plane with their long axes oriented along the *c*-axis, and they exhibited a herringbone arrangement with very similar herringbone and tilt angles. In the case of **1**, however, the packing symmetry in the *ab* plane was broken because the molecules formed N–H···O=C hydrogen-bonded chains along the crystallographic [110] direction. Each amide function was thus involved in two slightly different hydrogen-bonds (Supplementary Table S1). Most importantly, however, the volume per quaterthiophene unit in the quaterthiophene diacetamide was calculated to be 291 Å³ and, was, hence, significantly smaller than for **2** (308 Å³), as well as α-4T (307 Å³) or DH4T (306 Å³), that is, derivatives typically used in organic electronic devices (only DM4T with its entirely different intermolecular arrangement exhibited a comparable but still larger volume of 297 Å³ per quaterthiophene). Considering how remarkably similar the volume per quaterthiophene is for **2**, α-4T, and DH4T, despite the very different steric demand of their respective terminal substituents, it is tempting to assume that its value represents the "inherent" spatial requirements for a π–π stacked quaterthiophene as a result of Van der Waals and quadrupolar interactions. From the direct comparison with the diacetate **2**, the higher packing density in the case of **1** would hence appear to result from the additional hydrogen bonding interaction between the terminal acetamide substituents of **1**. Consistent with this noticeably denser packing in the unit cell, the distances between both the parallel-displaced π–π stacked neighbors and edge-to-face pairs were significantly reduced, as reflected by C···C, C···S and S···S short contacts that were smaller than for other quaterthiophene derivatives with a layered

herringbone packing, including reference compound **2** (Figure 1*d*).

DFT Computations of Electron Overlap Effects

We regard the higher packing density of the π-conjugated cores and the smaller short contacts in **1** as an important feature resulting from the hydrogen-bonded substituents, which could potentially result in an improved π-overlap and, consequently, better transport properties. In order to quantify the effect of packing density on the electronic structure of the investigated crystals, we developed an electronic compactness index based on the density overlap regions indicator (DORI).[50] As DORI is a density-based scalar field revealing regions of high-density overlap between atoms and molecules, the number of electrons encapsulated within an intermolecular DORI domain can be used to compare electronic overlap effects between corresponding sites in crystal lattices (Supplementary Figure S3). This new method has recently shown good correlation to experimental results and has the advantage of being less sensitive to small changes in the molecular geometry (e.g. DFT optimization level vs. experimental X-Ray structures) than the computation of charge transfer integrals. The compactness index was computed for different pairs of neighboring quaterthiophene cores within the *ab* plane, using the atom positions as determined for the crystal structures of **1**, **2**, α-4T, DM4T and D4HT (Figure 2). The DORI values for **1** were the highest of all quaterthiophenes for all pairs of nearest neighbors, with maximum values between edge-to-face pairs being more than 18% higher than for any of the reference compounds.

In marked contrast, the values for the non-hydrogen-bonded quaterthiophene diacetate **2** were comparatively low, which confirms that the formation of hydrogen bonds and the resulting

denser packing of the quaterthiophene cores plays a decisive role in electronic overlap.
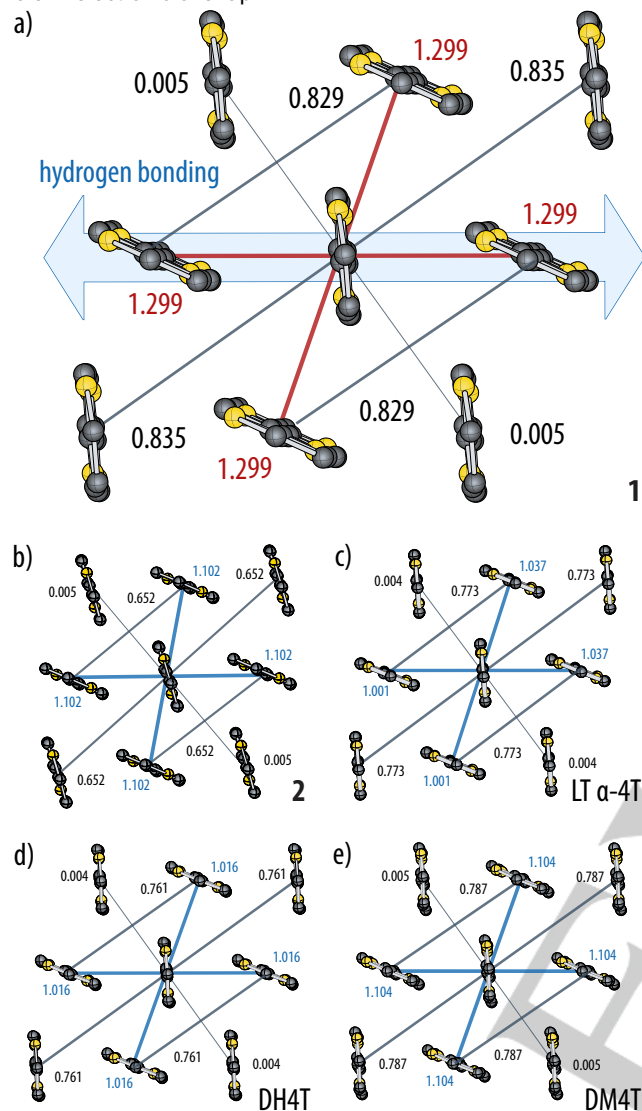
Figure 2. Top views onto the herringbone packing of the quaterthiophene cores in a) **1**, in comparison to b) **2**, c) LT,[42] α-4T, d) DM4T,[43] and e) DH4T[44] (all hydrogen atoms and side chains omitted for clarity). The numbers and line widths represent the computed density overlap regions indicator (DORI) values of quaterthiophene pairs.

Interestingly, the symmetry breaking of the two-dimensional herringbone packing within a quaterthiophene layer in **1**, caused by the intermolecular N–H···O=C hydrogen bonding, does not seem to be reflected in the compactness index, because the DORI values were identical for all edge-to-face dimers. Closer inspection revealed that this was in fact a coincidence, because the integration domains differed in volume for hydrogen-bonded (52.8 Å^3) and non-bonded (54.5 Å^3) dimers, resulting in the expected higher average electron density for the former one. Overall, the DORI results confirmed that hydrogen bonding in **1** induced a denser packing with improved π-interactions, as required for charge transport.

Thin Film Growth, Morphology, and Structure

Crystalline thin films of **1** suitable for the fabrication of organic field-effect transistors (OFETs) were prepared by physical vapor deposition at various substrate temperatures T_S = 20–140°C

onto three different types of substrates, that is, *(i)* bare p-doped silicon with a 200 nm thermal oxide layer (SiO$_2$), *(ii)* the same substrate covered with a self-assembled monolayer of octadecyltrichlorosilane (OTS), as well as *(iii)* p-doped silicon covered with a 200 nm Si$_3$N$_4$ layer. Atomic force microscopy (AFM) imaging on thin films deposited at T_S = 24°C on SiO$_2$ showed a high number of small, and supposedly amorphous grains with average diameters of 150 nm and heights of 1.5 nm covering the substrate (Supplementary Figure S4). By contrast, films obtained at higher substrate temperatures (T_S = 60–140°C) followed Stranski-Krastanov growth mechanism (Supplementary Figures S5). The first layers showed two-dimensional growth of continuous layers up to a certain threshold thickness, followed by three-dimensional growth of needle-like features with an average height of 20 nm protruding from the SiO$_2$ surface (Figure 3a, Supplementary Figure S6). The crystalline islands and terraces in thin films of **1** exhibited a uniform height of 2.7 nm, matching the interplanar distance between the *ab* layers observed in the single-crystal structure of **1**. Accordingly, these flat-on crystals were inferred to comprise monolayers of **1** with the molecular long axis "standing up" on the substrate. Upon increasing the substrate temperature during evaporation to 120°C, the nucleation density estimated from the AFM images decreased by almost three orders of magnitude, while the grain size increased to several micrometers (Supplementary Figure S7). Moreover, the second and subsequent layers appeared only to form only once the surface coverage by the previous layer was almost complete, suggesting that the layer edges may be preferential sites for the adsorption of new molecules. Furthermore, layer-by-layer two-dimensional (Frank-van der Merwe type) versus needle-like growth was strongly favored on both OTS-treated SiO$_2$ or Si$_3$N$_4$ substrates, as demonstrated by AFM (Figure 3b–f) and bright-field transmission electron microscopy (BF-TEM) imaging (Figure 3g–i).

In this way, micrometer-sized crystalline two-dimensional layers of **1** with a limited number of grain boundaries were obtained, originating either from a low nucleation density or coalescence of adjacent domains with the same orientation on the substrate. Occasionally, large needles were observed that, unlike those on SiO$_2$, extended parallel to the substrate and were composed of "edge-on" oriented lamellae according to high resolution TEM (HR-TEM) imaging (Figure 4a, Supplementary Figure S8). Notably, the thin films of **1** hence differed in their morphology from those of α-4T or DH4T thin films[51,52] by the remarkably straight grain/terrace boundaries of the micrometer-sized grains and the occurrence of needles. Previously, Campione et al. reported a similar coexistence of two-dimensional terraces and needles in certain α-4T thin films grown on potassium monohydrogen phthalate single crystals using either hot-wall or molecular epitaxy.[53]

In the present case, the pronounced morphological difference between films grown on bare SiO$_2$ and those obtained on OTS-treated surfaces (as well as Si$_3$N$_4$ substrates) indicates that a hydrophobic surface treatment is probably even because of the possible interaction of the hydrogen-bonded acetamide groups of **1** with hydrophilic surface functions. Selected-area electron and grazing incidence X-ray diffraction (SAED, GIXD) as well as X-ray reflectivity (XR) measurements confirmed that the dense packing observed in the single-crystal structure of **1** was preserved within the thin films.
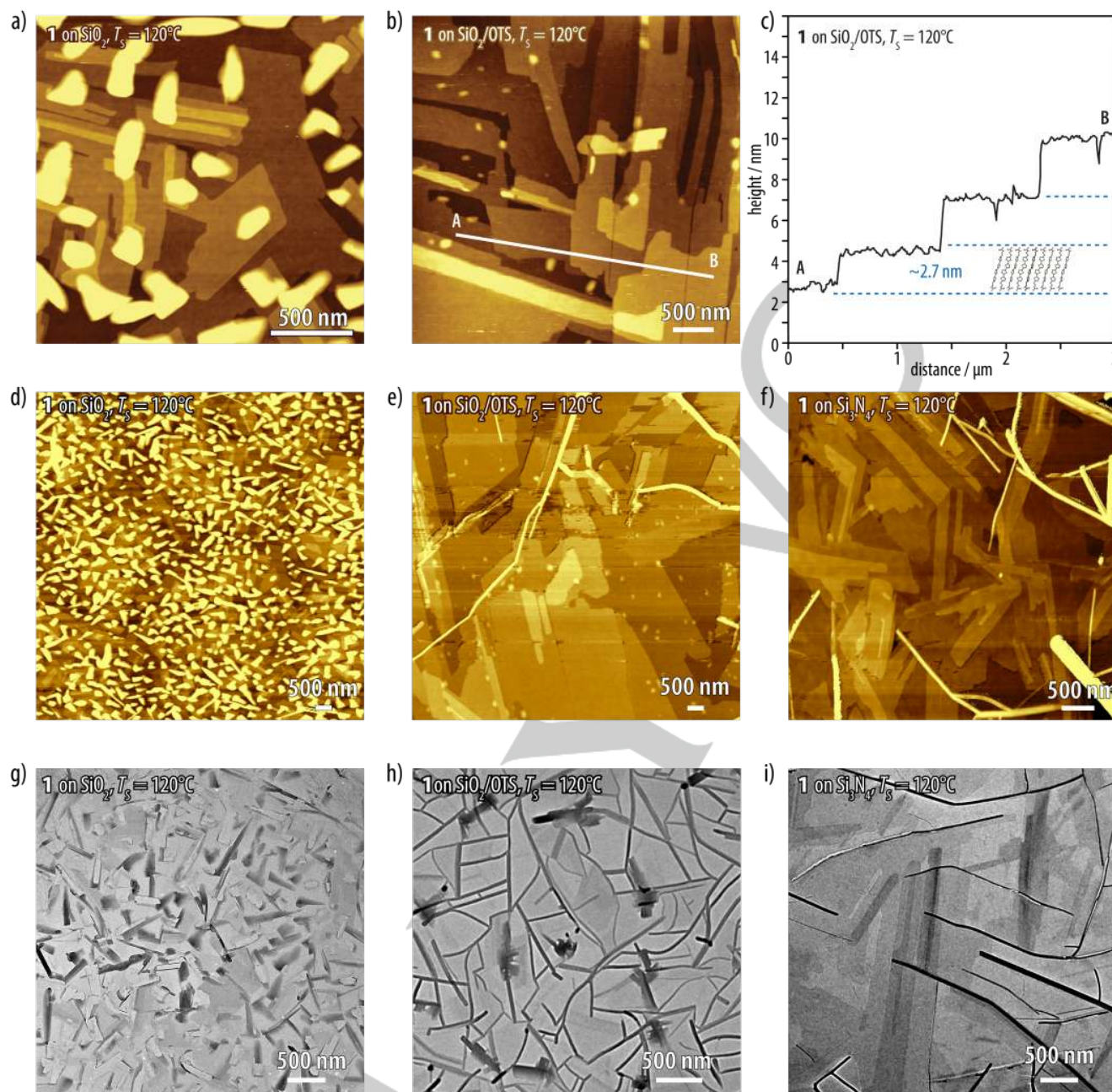
Figure 3. Atomic force microscopy (AFM) height images of films of 1 vapor-deposited onto *a*) Si⁺/SiO₂ or *b*) OTS-treated Si⁺/SiO₂ substrates, as well as *c*) a height profile obtained from the latter AFM image. *d–f*) Comparison of AFM images as well as *g–i*) bright-field transmission electron microscopy (BF-TEM) images of films of **1** vapor-deposited onto Si⁺/SiO₂, OTS-treated Si⁺/SiO₂ substrates, and Si₃N₄ substrates.

SAED of films grown on OTS-treated SiO₂ revealed mainly two patterns that, by comparison with calculated patterns from the single crystal structure, were attributed to a (001) contact plane within the 2D layers, and a (010) contact plane within the needles (Figure 4*b*, Supplementary Figure S9, Supplementary Table S2). This finding confirmed that the thin films were indeed constituted from layers of **1** with the molecular long axis "standing up" relative to the substrate. Accordingly, XR scans revealed the typical series of 00L diffraction peaks of vertically ordered thin films, exhibiting a period of $\Delta q_z = 0.243$ Å⁻¹ (Figure 5*a*), which corresponds to an interplanar distance $d_{001} = 2\pi/\Delta q_z \approx 25.9$ Å.

A typical GIXD pattern of films on OTS-treated substrates (Figure 5*b*, Supplementary Figure S10) showed peaks for a 2D powder with randomly oriented crystallites (as well as a peak corresponding to the long axis of **1**, attributed to the needles with a molecular orientation parallel to the substrate, consistent with SAED and HR-TEM). A detailed analysis of the diffraction map allowed us to index the peaks, resulting in a triclinic unit cell with lattice parameters of $a = 5.72$ Å, $b = 8.04$ Å, $c = 25.9$ Å and $\alpha = 97.2°$, $\beta = 89.8°$, and $\gamma = 90.1°$, in good agreement with the single crystal structure.
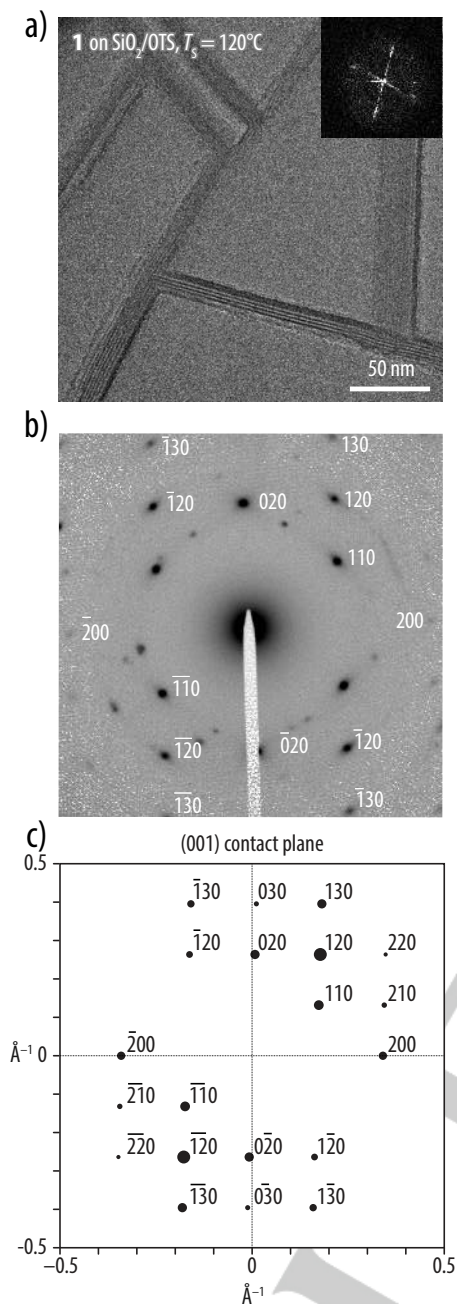
Figure 4. *a)* High-resolution transmission electron microscopy (HR-TEM) images of films of **1** deposited onto SiO$_2$/OTS at T_S = 120°; the inset shows the fast Fourier transformation (FFT) from the HR-TEM images, revealing a periodicity of approximately 26 Å for the needle-like domains. *b,c)* Representative selected-area electron diffraction (SAED) map of the films of **1** showing good agreement with the calculated diffraction map from the single crystal of **1** (see Supplementary Figure S9, Supplementary Table S1), indicating the coexistence of a (001) and (00−1) contact plane.

In particular, the close match of the *ab* area values indicate that the dense packing observed in the single crystal structure of **1** (45.0 Å^2) was retained in the thin films (46.0 Å^2). UV-vis absorption spectra of **1** deposited on fused silica (T_S = 120°C) revealed absorption maxima at 342 and 365 nm, of which the latter had not been observed for either α-4T or DH4T thin films, and they also exhibited a more pronounced fine-structure with shoulders at 401, 426, and 456 nm (Supplementary Figure S11).[52]
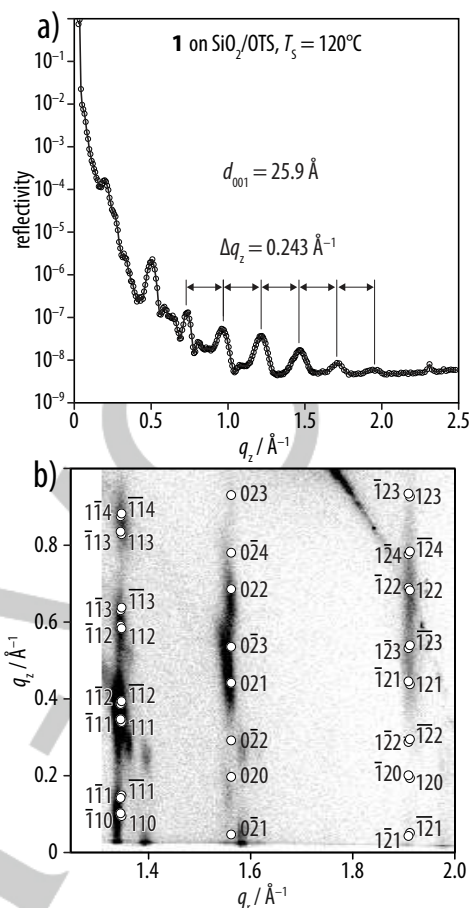
Figure 5. *a)* Specular X-ray reflectivity (XR) measurements revealed a series of 00L reflection peaks with a period of 0.243 Å^{-1}, corresponding to an interplanar distance of 25.9 Å. *b)* Detailed view onto the 11L, 02L, 12L diffraction series in the grazing incidence X-ray diffraction (GIXD) pattern, with the expected reflections indicated.

Both observations qualitatively showed that the electronic interactions of the quaterthiophenes **1** resulting from its packing in the thin films were indeed different from those of other quaterthiophenes.

Organic Field-Effect Transistors

Thin films of **1** vapor-deposited at elevated substrate temperatures, in particular, on OTS-treated or Si$_3$N$_4$ substrates exhibited a highly promising morphology and internal crystal structure for two-dimensional charge transport. Therefore, we fabricated bottom-gate top-contact organic field-effect transistors (OFETs) with channel lengths from L = 5–200 μm from thin films of **1** by thermal deposition of Au source and drain electrodes. The output curves as well as the transfer curves in the saturation regime (V_D = –60 V) were measured independently in an inert atmosphere, in order to obtain the field-effect mobilities μ, current on-off ratios I_{on}/I_{off}, and threshold voltages V_T (Table 2). All devices showed typical OFET characteristics for organic p-type semiconducting materials (Figure 6, Supplementary Figures S12–S13).

The devices prepared from thin films on bare SiO$_2$, with the exception of the sample obtained at a substrate temperature T_S = 24°C, exhibited mobilities $\mu \geq 10^{-3}$ cm^2 V^{-1} s^{-1} and I_{on}/I_{off} ratios of 10^3–10^5.

a)

b)

c)
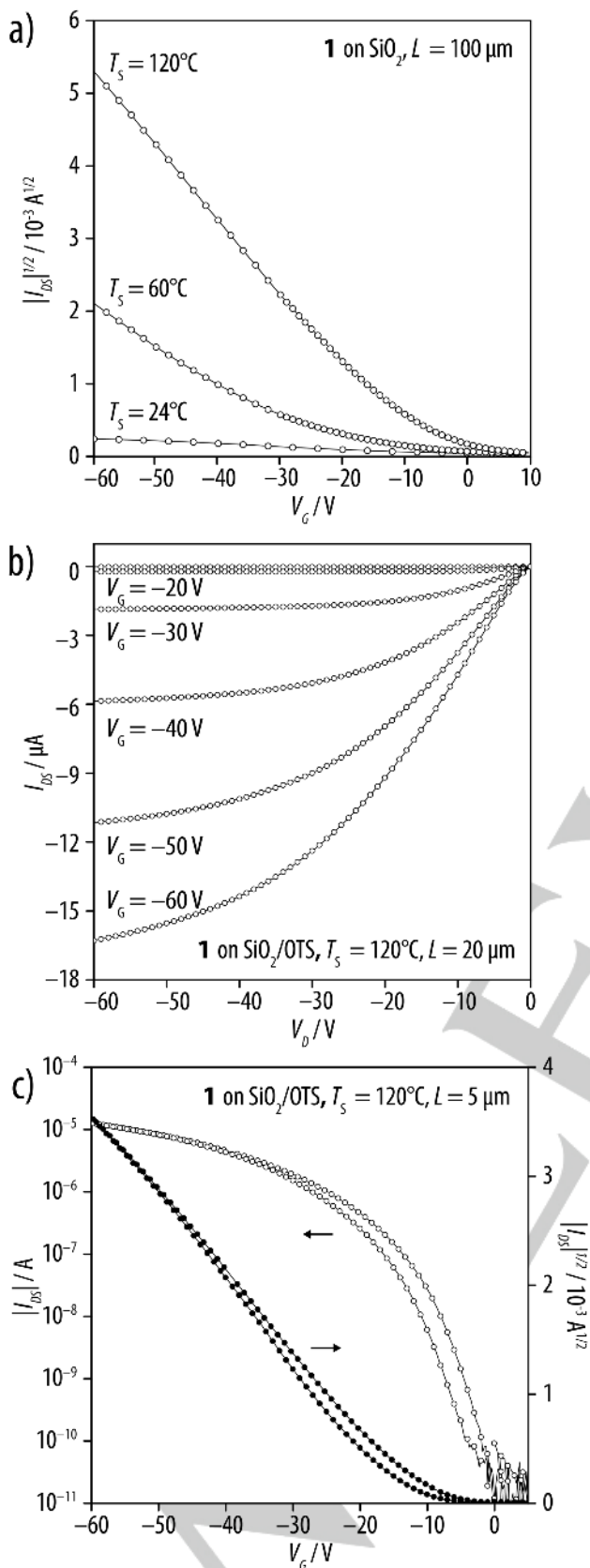
Figure 6. Representative examples of *a)* a directly measured transfer curve and *b)* output curves for the bottom-gate top-contact transistors fabricated from films of **1** on a bare or OTS-treated SiO₂ substrates. *c)* Transfer curves of devices fabricated from films of **1** on OTS-treated SiO₂ substrates, measured in the forward and reverse directions exhibited a small hysteresis. See Supplementary Figures S12–S13 for details.

The overall highest mobilities and on-off ratios were observed at substrate temperatures $T_S \approx 120°C$. Devices prepared on OTS-treated substrates showed a significantly better performance by all measures than those on bare SiO₂ substrates. Thin films deposited at 120°C on OTS-treated substrates had average mobilities of up to 0.18 cm² V⁻¹ s⁻¹, which is the same range as the highest mobilities previously reported for single-crystalline specimen.[45–47,54] Moreover, the devices exhibited good on-off ratios of $I_{on}/I_{off} = 10^5$ as well as improved threshold voltages compared to devices on bare SiO₂ substrates. The still large threshold voltages show that there is room for device optimization even in the case of the OTS-treated substrates. Nevertheless, it is important to note that only a small hysteresis behavior was observed when measuring the transfer characteristics in the forward and reverse directions (Figure 6*c*, Supplementary Figure S13). This implies that the hydrogen-bonded substituents in quaterthiophene **1** are not a major source of trap states.

When the optimal deposition conditions used for **1** ($T_S \approx 120°C$ on OTS-treated substrates) were then employed for the reference compound quaterthiophene **2**, the obtained thin films were not continuous and exhibited islands, according to AFM imaging (Supplementary Figure S14). Consequently, transistors fabricated from these thin films showed no detectable current. Given the obvious differences in thermal properties of **1** and **2** in thermogravimetric analysis (TGA) and differential scanning calorimetry (DSC), we found substrate temperatures as low as $T_S \approx 40°C$ to result in an almost complete coverage of the substrate with a homogeneous film (Supplementary Figure S14). Transistors prepared from these thin films resulted in average mobilities of up to 6.6 · 10⁻³ cm² V⁻¹ s⁻¹, which is almost two orders of magnitude lower than those observed for **1** (Table 2, Supplementary Figure S15).

Conclusions

In conclusion, we found that OFET devices fabricated from polycrystalline thin films of the quaterthiophene acetamide **1** exhibited a performance on the level of devices from quaterthiophene single-crystals. We attribute this finding to the introduction of hydrogen-bonded terminal substituents as an additional structure-directing element. In order for this interaction to positively impact OFET performance, it should not disrupt but promote the formation of extended layered structures parallel to the plane of the substrate with the preferred herringbone arrangement of the calamitic π-conjugated cores, which is favorable for two-dimensional charge transport. A simple but crucial element in this regard is the short flexible spacer between the hydrogen-bonded substituents and the core, which decouples the conflicting geometric requirements of the herringbone arrangement and hydrogen bonding. In this way, the dispersive and quadrupolar contributions to the π-interactions can be optimized by way of the herringbone arrangement of the cores, while hydrogen bonding within the arrays of the amide groups along one lattice axis parallel to the substrate provides an additional incentive for fast in-plane crystal growth, similar to how the formation of well-defined nanowires comprising tightly π–π stacked chromophores is promoted by synergistic lateral hydrogen bonding.[29] This is possible because the *ab* lattice parameters in a typical herringbone arrangement (of about 10 Å) are similar to the

intermolecular distance enforced by the N–H···O=C hydrogen bonding (of typically 9.2–9.8 Å over two molecules). Since the latter is in fact smaller, the hydrogen-bonded side groups, moreover, induce a tighter packing of the molecules in the crystal structure. On an appropriate substrate surface, the overall result is the formation of two-dimensional layers with larger domain sizes, higher internal crystalline order, and a tighter packing of the calamitic π-conjugated pores in both dimensions, which results in a larger π-overlap, as compared to the reference compound **2**. Consistent with these structural differences, we observed average field-effect mobilities that are almost two orders of magnitude higher than those observed for **2**. Moreover, these mobilities were in the range of the best values

previously reported for single-crystalline quaterthiophene specimens.[45–47] The still moderate absolute mobility values certainly reflect the fact that quaterthiophenes are comparably poor organic semiconductors, and other factors such as surface treatment and processing are very important for device performance, as well.[55] Nevertheless, our results demonstrate that hydrogen bonding is not only compatible with charge transport in p-type organic semiconductors but reinforces the structural elements required for good π-overlap. Hence, the use of hydrogen-bonded side groups will provide a general pathway for novel organic semiconductors such as semiconducting polyamides with improved morphology and device performance.[56]

Table 2. Average mobilities μ (and maximum mobilities μ_{max} in brackets),[a] on/off ratios I_{on}/I_{off}, and threshold voltages V_T of bottom-gate (Si$^+$) top-contact (Au) OFETs fabricated from **1** and **2**; entries 1–7: variation of substrate temperature T_S; entries 8–18: variation of channel length and active materials for devices on bare and OTS-treated SiO$_2$ substrates; entries 17–18: devices on Si$_3$N$_4$. All devices were measured in an inert atmosphere.

entry	material	gate dielectric	T_S	film thickness	L	W	μ (μ_{max})	I_{on} / I_{off}	V_T
			(°C)	(Å)	(μm)	(μm)	(cm^2 V^{-1} s^{-1})		(V)
1	**1**	SiO$_2$	24	100	100	6000	$3.5 \cdot 10^{-5}$	10^2	−4
2	**1**	SiO$_2$	60	300	100	6000	$6.1 \cdot 10^{-3}$	10^3	−25
3	**1**	SiO$_2$	100	400	100	6000	$1.8 \cdot 10^{-3}$	10^3	5
4	**1**	SiO$_2$	120	500	100	6000	$1.8 \cdot 10^{-2}$	10^4–10^5	−9
5	**1**	SiO$_2$	125	600	100	6000	$1.7 \cdot 10^{-2}$	10^3	−17
6	**1**	SiO$_2$	135	600	100	6000	$6.8 \cdot 10^{-3}$	10^3	−10
7	**1**	SiO$_2$	140	650	100	6000	$5.5 \cdot 10^{-3}$	10^3	−5
8[a]	**1**	SiO$_2$	120	650	20	200	$7.4 \pm 0.62 (8.5) \cdot 10^{-3}$	10^3–10^4	−36 (± 2)
9[a]	**1**	SiO$_2$	120	650	10	100	$4.7 \pm 1.04 (6.1) \cdot 10^{-3}$	10^3–10^4	−37 (± 8)
10[a]	**1**	SiO$_2$	120	650	5	50	$8.9 \pm 1.59 (11.4) \cdot 10^{-3}$	10^3–10^4	−30 (± 6)
11[a]	**2**	SiO$_2$/OTS	40	650	20	200	$1.7 \pm 0.24 (1.9) \cdot 10^{-3}$	10^3–10^4	−26 (± 11)
12[a]	**2**	SiO$_2$/OTS	40	650	10	100	$6.6 \pm 2.89 (8.7) \cdot 10^{-3}$	10^4	−21 (± 4)
13[a]	**2**	SiO$_2$/OTS	40	650	5	50	$2.4 \pm 1.46 (5.3) \cdot 10^{-3}$	10^4	−28 (± 7)
14[a]	**1**	SiO$_2$/OTS	120	650	20	200	$1.4 \pm 0.14 (1.5) \cdot 10^{-1}$	10^5	−24 (± 6)
15[a]	**1**	SiO$_2$/OTS	120	650	10	100	$1.8 \pm 0.23 (2.1) \cdot 10^{-1}$	10^5	−21 (± 3)
16[a]	**1**	SiO$_2$/OTS	120	650	5	50	$0.6 \pm 0.06 (0.8) \cdot 10^{-1}$	>10^5	−18 (± 12)
17	**1**	Si$_3$N$_4$	120	650	200	600	$7.5 \cdot 10^{-3}$	10^3	−25
18	**1**	Si$_3$N$_4$	120	650	100	600	$8.3 \cdot 10^{-3}$	10^2	−21

[a] The reported device characteristics were averaged out over three to five devices from two different batches.

Experimental Section

Materials and Methods

Materials. The synthetic precursors 2-(5-bromo-2-thienyl)ethyl acetate and 5,5'-bis(tributylstannyl)-2,2'-bithiophene, were prepared as reported in the literature.[48,57] Heavily boron-doped silicon wafers (Si⁺) with a thermal oxide layer of 200 nm, 525 µm thick and with a capacitance c_{ox} of 19.5 nF/cm² were purchased from the *Center of Micronanotechnology* at EPFL. These wafers were used without further treatment as substrates for the fabrication of thin films of **1** and **2**. Treatment of the SiO₂ substrates with octadecyltrichlorosilane (OTS) was performed in a glovebox by immersing the silicon wafers into a solution of 15 mg OTS in 5 mL of toluene at 65–70 °C for 10 min followed by rinsing with isopropanol. Contact angles of approximately 110° were obtained after the treatment. Heavily boron-doped silicon wafers (Si⁺) with a Si₃N₄ layer of 200 nm were purchased from the *Center of Micronanotechnology* at EPFL.

Synthesis, Purification and Single Crystal Growth of 1. The quaterthiophene bisacetamide **1** was synthesized as described previously.[48] Single crystals of **1** suitable for X-ray crystal structure analysis were obtained by high vacuum sublimation at 10⁻⁷ mbar at temperatures of 240–260°C over 3–4 weeks. This material was then also used for the fabrication of thin films of **1**.

Synthesis, Purification and Single Crystal Growth of 2. 2-(5-bromo-2-thienyl)ethyl acetate (3.43 g, 13.77 mmol) and 5,5'-bis(tributylstannyl)-2,2'-bithiophene (5.00 g, 6.72 mmol) were dissolved in 50 mL DMF in an inert atmosphere in a well-dried 100 mL Schlenk flask. Tetrakis(triphenylphosphine)palladium (35 mg, 0.03 mmol) was added, and the reaction mixture was stirred overnight at 80 °C. After allowing the mixture to cool to room temperature, an orange precipitate formed that was filtered off and washed with diisopropylether (150 mL) as well as diethylether (50 mL). The residue was dried in vacuum and purified by column chromatography (silica gel, DCM/heptane 4:1). The product was isolated as a yellow powder in 55% yield (1.87 g). Single crystals of **2** suitable for X-ray crystal structure analysis were grown from a toluene solution by slow evaporation at room temperature over 3–4 weeks. ¹H NMR (400.13 MHz, CD₂Cl₂): δ = 2.06 (s, 6H, 2 CH₃), 3.13 (t, J = 6.6 Hz, 4H, 2 CH₂), 4.28 (t, J = 6.6 Hz, 4H, 2 CH₂), 6.80 (d, J = 3.8 Hz, 2H, Ar-H), 7.02-7.06 (m, 4H, Ar-H), 7.08 (d, J = 3.8 Hz, 2H, Ar-H); ¹³C NMR (100.62 MHz, CD₂Cl₂): δ = 20.63, 29.43, 64.16, 123.47, 123.88, 124.14, 126.40, 135.39, 135.41, 136.31, 139.99, 170.55; HRMS (APCI): calcd C₂₄H₂₂O₄S₄ ([M]⁺) 503.0479; found 503.0477; R_f (DCM/heptane 4:1): 0.25.

Thermal Characterization. Thermogravimetric analysis (TGA) scans were recorded using a Perkin Elmer TGA 4000. The specimens (5–10 mg) were dried in high vacuum at 80 °C for 24 h and then heated from 30 °C to 950 °C at a scanning rate of 10 °C/min in a flow of nitrogen (20 mL/min). Differential scanning calorimetry (DSC) was carried out with a TA Instruments Q100 calorimeter at a scanning rate of 10°C/min under nitrogen flow (50 mL/min). Specimens of about 3–5 mg were first heated to a temperature 20 °C above their melting point and then cooled to 0 °C at a cooling rate of –10 °C/min in order to erase the effects of their thermal history. The data given for the thermal transitions were obtained from the second heating and first cooling scans.

X-ray Crystallography. The data collection for compound **1** (CCDC 976399) and compound **2** was performed at low temperatures [140(2) K, and 100(2) K] using Cu and Mo K_α radiation on an Agilent Technologies SuperNova dual system in combination with an Atlas CCD detector, respectively (Supplementary Table S3–S6). The data reduction was carried out by Crysalis PRO.[58] The solution and refinement were performed by SHELX.[59] The crystal structure was refined using full-matrix least-squares based on F^2 with all non-hydrogen atoms anisotropically refined. Hydrogen atoms were placed in calculated positions by means of the "riding" model. In the final stages of refinement, the crystal structure showed clear signs of disorder that was treated by means of the split model and by applying some restraints to some atomic displacement parameters (SIMU card) and to some bond distances (SADI card) in order to obtain reasonable values.

Computational Details. Pairs of molecules were extracted from the five crystal structures of **1**, **2**, α-4T, DM4T, and DH4T. The lateral chains were removed, and hydrogen atoms positions were optimized at the B3LYP/6-31G(d) level in Gaussian 09.[60] The electron density was calculated at B3LYP/TZP level in ADF2013.[61–63] The DORI-based electronic compactness index was computed in locally modified version of DGrid.[64] The compactness index was computed as integral of the electron density over the intermolecular regions as reported previously.[50]

Thin Film Deposition. The SiO₂, SiO₂/OTS, or Si₃N₄ substrates were heated to the desired substrate temperatures T_S = 24–140°C in high vacuum (10⁻⁷ mbar) overnight prior to quaterthiophene deposition. Deposition of compounds **1** and **2** was monitored using a quartz crystal microbalance, and the deposition rate was maintained constant at around 3 Å/min. The distance between the alumina crucible charged with **1** and the sample holder was around 40 cm.

Atomic Force Microscopy. AFM images were obtained in tapping mode using a Nanoscope IIIa (Veeco Instruments Inc., Santa Barbara, USA) instrument or a NT–MDT Solver Pro with a SMENA scanner at room temperature in air. Cantilevers with an average resonance frequency of f_0 = 75 or 150 kHz and k = 3.5 or 5 Nm⁻¹ were used, respectively. Scan rates of 0.1–2.0 Hz were applied, and the image resolution was 512 × 512 pixels. The images were processed using the Gwyddion software package.

Transmission Electron Microscopy and Electron Diffraction. Films of **1** were coated with a thin amorphous carbon film, and the carbon-coated film was removed from the SiO₂ substrate by using poly(acrylic acid) (25% aqueous solution, Aldrich). Subsequently the thin films were recovered onto TEM copper grids by floating them on water. TEM was performed in bright field, high resolution, dark field and diffraction modes using a CM12 Philips microscope (120 kV) equipped with a MVIII (Soft Imaging System) charge coupled device camera. The high-resolution TEM images were acquired in a modified low-dose mode and afterwards treated as described in the literature.[65] The calculation of the electron diffraction patterns for **1** was realized using the diffraction module of the Cerius² software (Accelrys).

Grazing Incidence X-Ray Diffraction. Grazing Incidence X-ray Diffraction (GIXD) experiments were performed at beamline ID10 at the European Synchrotron Radiation Facility in Grenoble using 22 keV X-rays. The grazing angle α was set to 0.080°, i.e., just below the critical angle of silicon, α_c = 0.082, which corresponds to q_c = 0.032 Å⁻¹. Hence, the incident wave experiences total external reflection, and only the evanescent wave probes the sample. In this configuration, the scattered intensity by the surface is maximized, whereas the bulk scattering is reduced.[66,67] The data was collected with a Pilatus 300K area detector with an illumination time of 1 s. In this geometry, the momentum transfer vector has a vertical and horizontal component, $q_z = 2\pi/\lambda \cdot (\sin\alpha + \sin\beta)$ and $q_r = 4\pi/\lambda \cdot (\sin 2\theta/2)$, respectively, with the outgoing angle β and the horizontal scattering angle 2θ. Note that the present thin films consist of crystallites randomly oriented in the plane, so that any Bragg peak can be merely found by mapping the (2θ, β)-space.[68]

X-Ray Reflectivity. Specular X-ray reflectivity (XR) measurements were performed at beamline ID10 at the European Synchrotron Radiation Facility in Grenoble using 22 keV X-rays. XR was measured with the detector placed in the reflection plane and outgoing angle β equal to incoming angle α with a scintillation detector and counting times of 1 s per point. In this geometry, the momentum transfer vector is normal to the surface, $q_z = 4\pi/\lambda \cdot \sin\alpha$. The reflected intensity was measured as a function of q_z, and was normalized to the incident intensity. The resulting reflectivity curves $R(q_z)$ are sensitive to the surface normal electron density profile and, hence, allow for a determination of the periodicity of layered systems perpendicular to substrates surface. [69,70]

OFET Device Fabrication. Bottom-gate top-contact transistors were fabricated from thin films of **1** and **2** via thermal deposition of Au source and drain electrodes (80 nm) in high vacuum (10^{-6} mbar) and at a substrate temperature of –185°C through different shadow masks. Long channel transistors with channel lengths L = 100, 200 and a channel width W of 6 mm were patterned using a steel shadow mask. Short channel transistors with channel lengths L = 5, 10, or 20 µm and an aspect ratio W/L = 10 were patterned by stencil masks made of low-stress Si_3N_4 membranes supported by bulk Si. These stencils were fabricated in the *Microsystems Laboratory 1* of Prof. J. Brugger at EPFL.[71,72]

OFET Characterization. The transfer characteristics of all transistor devices were recorded directly by measuring the channel current I_{DS} in dependence of the gate voltage V_G in the saturation regime of the transistor (V_D = –60 V or V_D =–40 V) in an inert atmosphere (N_2 or Ar) and at ambient temperature using a Keithley 4200 semiconductor characterization system or a Keithley 2612a dual-channel source measure unit. All measurements were performed at scan rates of 0.25–0.5 V/s. The field effect mobility μ in the saturation regime was extracted from the slope and the threshold voltage V_T from the V_G-axis interception of a linear fit of the square root of the absolute saturation drain current I_{DS} as a function of the gate voltage V_G, according to $I_{DS} = (W/2L)\, C_i\, \mu\, (V_G - V_T)^2$.

Acknowledgements

[1] Braga Daniele, Horowitz Gilles, *Advanced Materials* **2009**, *21*, 1473–1486.

[2] A. R. Murphy, J. M. J. Fréchet, *Chem. Rev.* **2007**, *107*, 1066–1096.

[3] C. Wang, H. Dong, W. Hu, Y. Liu, D. Zhu, *Chem. Rev.* **2012**, *112*, 2208–2267.

[4] A. F. Paterson, S. Singh, K. J. Fallon, T. Hodsden, Y. Han, B. C. Schroeder, H. Bronstein, M. Heeney, I. McCulloch, T. D. Anthopoulos, *Advanced Materials* **2018**, *30*, 1801079.

[5] X. Zhan, A. Facchetti, S. Barlow, T. J. Marks, M. A. Ratner, M. R. Wasielewski, S. R. Marder, *Advanced Materials* **2011**, *23*, 268–284.

[6] M. C. Gather, A. Köhnen, K. Meerholz, *Advanced Materials* **2011**, *23*, 233–248.

[7] P. Lin, F. Yan, *Advanced Materials* **2012**, *24*, 34–51.

[8] Y. Guo, G. Yu, Y. Liu, *Advanced Materials* **2010**, *22*, 4427–4447.

[9] G. Zhao, H. Dong, Q. Liao, J. Jiang, Y. Luo, H. Fu, W. Hu, *Nat Commun* **2018**, *9*, 4790.

[10] A. Mishra, C.-Q. Ma, P. Bäuerle, *Chem. Rev.* **2009**, *109*, 1141–1276.

[11] I. Vladimirov, M. Kellermeier, T. Geßner, Z. Molla, S. Grigorian, U. Pietsch, L. S. Schaffroth, M. Kühn, F. May, R. T. Weitz, *Nano Lett.* **2018**, *18*, 9–14.

[12] R. Noriega, J. Rivnay, K. Vandewal, F. P. V. Koch, N. Stingelin, P. Smith, M. F. Toney, A. Salleo, *Nature Materials* **2013**, *12*, 1038–1044.

[13] G. R. Desiraju, *Accounts of chemical research* **2002**, *35*, 565–573.

[14] T. Steiner, *Angew. Chem. Int. Ed.* **2002**, *41*, 48–76.

[15] R. Custelcean, *Chemical Society Reviews* **2010**, *39*, 3675–3685.

[16] T. L. Nguyen, F. W. Fowler, J. W. Lauher, *Journal of the American Chemical Society* **2001**, *123*, 11057–11064.

[17] Jahnke Eike, Lieberwirth Ingo, Severin Nikolai, Rabe Jürgen P., Frauenrath Holger, *Angewandte Chemie International Edition* **2006**, *45*, 5383–5386.

[18] L. Tian, R. Szilluweit, R. Marty, L. Bertschi, M. Zerson, E.-C. Spitzner, R. Magerle, H. Frauenrath, *Chemical Science* **2012**, *3*, 1512–1521.

[19] R. J. Hafner, L. Tian, J. C. Brauer, T. Schmaltz, A. Sienkiewicz, S. Balog, V. Flauraud, J. Brugger, H. Frauenrath, *ACS Nano* **2018**, *12*, 9116–9125.

[20] S. Bauer, M. Kaltenbrunner, *Nature* **2016**, *539*, 365–367.

[21] A. Dell'Aquila, P. Mastrorilli, C. F. Nobile, G. Romanazzi, G. P. Suranna, L. Torsi, M. C. Tanese, D. Acierno, E. Amendola, P. Morales, *J. Mater. Chem.* **2006**, *16*, 1183.

[22] N. B. Kolhe, R. N. Devi, S. P. Senanayak, B. Jancy, K. S. Narayan, S. K. Asha, *Journal of Materials Chemistry* **2012**, *22*, 15235.

[23] S.-M. Jeong, T.-G. Kim, E. Jung, J.-W. Park, *ACS Appl. Mater. Interfaces* **2013**, *5*, 6837–6842.

[24] S. Kawano, N. Fujita, S. Shinkai, *Chemistry – A European Journal* **2005**, *11*, 4735–4742.

[25] B. D. Wall, S. R. Diegelmann, S. Zhang, T. J. Dawidczyk, W. L. Wilson, H. E. Katz, H.-Q. Mao, J. D. Tovar, *Advanced Materials* **2011**, *23*, 5009–5014.

[26] D. A. Stone, L. Hsu, S. I. Stupp, *Soft Matter* **2009**, *5*, 1990–1993.

[27] S. Yagai, T. Seki, H. Murayama, Y. Wakikawa, T. Ikoma, Y. Kikkawa, T. Karatsu, A. Kitamura, Y. Honsho, S. Seki, *Small* **2010**, *6*, 2731–2740.

[28] E.-K. Schillinger, E. Mena-Osteritz, J. Hentschel, H. G. Börner, P. Bäuerle, *Advanced Materials* **2009**, *21*, 1562–1567.

[29] R. Marty, R. Szilluweit, A. Sánchez-Ferrer, S. Bolisetty, J. Adamcik, R. Mezzenga, E.-C. Spitzner, M. Feifer, S. N. Steinmann, C. Corminboeuf, et al., *ACS Nano* **2013**, *7*, 8498–8508.

[30] R. Marty, R. Nigon, D. Leite, H. Frauenrath, *J. Am. Chem. Soc.* **2014**, *136*, 3919–3927.

[31] F. S. Schoonbeek, J. H. van Esch, B. Wegewijs, D. B. A. Rep, M. P. de Haas, T. M. Klapwijk, R. M. Kellogg, B. L. Feringa, *Angewandte Chemie International Edition* **1999**, *38*, 1393–1397.

[32] H. T. Black, N. Yee, Y. Zems, D. F. Perepichka, *Chemistry - A European Journal* **2016**, *22*, 17251–17261.

[33] C. Fu, P. J. Beldon, D. F. Perepichka, *Chemistry of Materials* **2017**, *29*, 2979–2987.

[34] M.-X. Zhang, G.-J. Zhao, *ChemSusChem* **2012**, *5*, 879–887.

[35] H. T. Black, D. F. Perepichka, *Angewandte Chemie International Edition* **2014**, *53*, 2138–2142.

[36] M. Gsänger, J. H. Oh, M. Könemann, H. W. Höffken, A.-M. Krause, Z. Bao, F. Würthner, *Angewandte Chemie International Edition* **2010**, *49*, 740–743.

[37] J. Yao, C. Yu, Z. Liu, H. Luo, Y. Yang, G. Zhang, D. Zhang, *Journal of the American Chemical Society* **2016**, *138*, 173–185.

[38] E. Daniel Głowacki, L. Leonat, M. Irimia-Vladu, R. Schwödiauer, M. Ullah, H. Sitter, S. Bauer, N. Serdar Sariciftci, *Appl. Phys. Lett.* **2012**, *101*, 023305.

[39] Y. Kanbur, H. Coskun, E. D. Głowacki, M. Irimia-Vladu, N. S. Sariciftci, C. Yumusak, *Organic Electronics* **2019**, *66*, 53–57.

[40] Głowacki Eric Daniel, Romanazzi Giuseppe, Yumusak Cigdem, Coskun Halime, Monkowius Uwe, Voss Gundula, Burian Max, Lechner Rainer T., Demitri Nicola, Redhammer Günther J., et al., *Advanced Functional Materials* **2015**, *25*, 776–787.

[41] E. D. Głowacki, M. Irimia-Vladu, M. Kaltenbrunner, J. Gsiorowski, M. S. White, U. Monkowius, G. Romanazzi, G. P. Suranna, P. Mastrorilli, T. Sekitani, et al., *Advanced Materials* **2013**, *25*, 1563–1569.

[42] T. Siegrist, C. Kloc, R. A. Laudise, H. E. Katz, R. C. Haddon, *Advanced Materials* **1998**, *10*, 379–382.

[43] S. Hotta, K. Waragai, *Journal of Materials Chemistry* **1991**, *1*, 835–842.

[44] M. Moret, M. Campione, A. Borghesi, L. Miozzo, A. Sassella, S. Trabattoni, B. Lotz, A. Thierry, *Journal of Materials Chemistry* **2005**, *15*, 2444–2449.

[45] H. E. Katz, A. J. Lovinger, J. G. Laquindanum, *Chemistry of Materials* **1998**, *10*, 457–459.

[46] Mannsfeld S. C. B., Locklin J., Reese C., E. Roberts M., Lovinger A. J., Bao Z., *Advanced Functional Materials* **2007**, *17*, 1617–1622.

[47] Reese Colin, Roberts Mark E., Parkin Sean R., Bao Zhenan, *Advanced Materials* **2009**, *21*, 3678–3681.

[48] Gebers Jan, Rolland Damien, Marty Roman, Suàrez Stéphane, Cervini Luca, Scopelliti Rosario, Brauer Jan Cornelius, Frauenrath Holger, *Chemistry – A European Journal* **2014**, *21*, 1542–1553.

[49] D. J. Skrovanek, P. C. Painter, M. M. Coleman, *Macromolecules* **1986**, *19*, 699–705.

[50] P. de Silva, C. Corminboeuf, *Journal of Chemical Theory and Computation* **2014**, *10*, 3745–3756.

[51] J. Ackermann, C. Videlot, P. Raynal, A. El Kassmi, P. Dumas, *Applied Surface Science* **2003**, *212–213*, 26–32.

[52] J. Ackermann, C. Videlot, P. Dumas, A. El Kassmi, R. Guglielmetti, V. Safarov, *Organic Electronics* **2004**, *5*, 213–222.

[53] M. Campione, A. Sassella, M. Moret, A. Papagni, S. Trabattoni, R. Resel, O. Lengyel, V. Marcon, G. Raos, *J. Am. Chem. Soc.* **2006**, *128*, 13378–13387.

[54] L. Zhang, N. S. Colella, B. P. Cherniawski, S. C. B. Mannsfeld, A. L. Briseno, *ACS Appl. Mater. Interfaces* **2014**, *6*, 5327–5343.

[55] Y. Yuan, G. Giri, A. L. Ayzner, A. P. Zoombelt, S. C. B. Mannsfeld, J. Chen, D. Nordlund, M. F. Toney, J. Huang, Z. Bao, *Nature Communications* **2014**, *5*, 3005.

[56] B. Özen, N. Candau, C. Temiz, F. C. Grozema, F. Fadaei Tirani, R. Scopelliti, J.-M. Chenal, C. J. G. Plummer, H. Frauenrath, *J. Mater. Chem. C* **2020**, 10.1039.C9TC06544J.

[57] L. Jiang, R. C. Hughes, D. Y. Sasaki, *Chem. Commun.* **2004**, *35*, DOI 10.1002/chin.200436094.

[58] *A.T.Crysalis PRO, Release 1.171.36.28*, **2013**.

[59] G. M. Sheldrick, *SHELXS/L-97, Program for the Solution/Refinement of Crystal Structures*, University Of Göttingen, Germany, **1997**.

[60] M. J. Frisch, G. W. Trucks, H. B. Schlegel, G. E. Scuseria, M. A. Robb, J. R. Cheeseman, G. Scalmani, V. Barone, B. Mennucci, G. A. Petersson, et al., *Gaussian ~09 Revision E.01*, **2009**.

[61] G. te Velde, F. M. Bickelhaupt, E. J. Baerends, C. F. Guerra, S. J. A. van Gisbergen, J. G. Snijders, T. Ziegler, *Journal of Computational Chemistry* **2001**, *22*, 931–967.

[62] C. Fonseca Guerra, J. G. Snijders, G. te Velde, E. J. Baerends, *Theoretical Chemistry Accounts: Theory, Computation, and Modeling (Theoretica Chimica Acta)* **1998**, *99*, 391–403.

[63] *Theoretical Chemisty Vrije Unversiteit Amsterdam, The Netherlands* **2013**.

[64] *Kohout, M., DGrid, Version 4.6, Radebeul*, **2011**.

[65] M. Brinkmann, P. Rannou, *Macromolecules* **2009**, *42*, 1125–1130.

[66] B. M. Ocko, X. Z. Wu, E. B. Sirota, S. K. Sinha, O. Gang, M. Deutsch, *Phys. Rev. E* **1997**, *55*, 3164–3182.

[67] G. H. Vineyard, *Phys. Rev. B* **1982**, *26*, 4146–4159.

[68] J. Als-Nielsen, D. Jacquemain, K. Kjaer, F. Leveiller, M. Lahav, L. Leiserowitz, *Physics Reports* **1994**, *246*, 251–313.

[69] A. Gibaud, S. Hazra, *SURFACE CHARACTERIZATION* **2000**, *78*, 11.

[70] L. G. Parratt, *Phys. Rev.* **1954**, *95*, 359–369.

[71] K. Sidler, N. V. Cvetkovic, V. Savu, D. Tsamados, A. M. Ionescu, J. Brugger, *Sensors and Actuators A: Physical* **2010**, *162*, 155–159.

[72] F. D. Fleischli, K. Sidler, M. Schaer, V. Savu, J. Brugger, L. Zuppiroli, *Organic Electronics* **2011**, *12*, 336–340.

FULL PAPER

Entry for the Table of Contents (Please choose one layout)

Layout 1:

FULL PAPER

Side-Chain Engineering via Hydrogen Bonding. Hydrogen-bonded substituents serve as an additional structure-directing element that helps to control the packing of the quaterthiophene with larger π-overlap, improves crystalline order, and results in larger domain sizes compared to related molecules without hydrogen-bonded substituents. These factors in turn reflected as an improved performance of the thin films in organic field effect transistors that is on par with that of single crystals of related quaterthiophene derivatives.
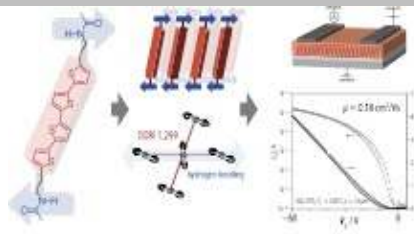
Author(s), Jan Gebers, Bilal Özen, Lucia Hartmann, Michel Schaer, Stéphane Suàrez, Philippe Bugnon, Rosario Scopelliti, Hans-Georg Steinrück, Oleg Konovalov, Andreas Magerl, Martin Brinkmann, Riccardo Petraglia, Piotr de Silva, Clémence Corminboeuf, and Holger Frauenrath,*

Page No. – Page No.

The Beneficial Role of Hydrogen Bonding for the Crystallization and OFET Performance of a Quaterthiophene Diacetamide